


ORIGINAL ARTICLE

Microstructure and corrosion resistance of hafnium-doped aluminide layers deposited on IN 713C nickel alloy using CVD method: experimental and ab initio studies

R. Sitek¹  · J. Kamiński¹ · A. Wadowski^{1,2} · M. Kopec³ · B. Adamczyk-Cieślak¹ · P. Bazarnik¹ · M. Drajewicz⁴ · W. J. Nowak⁴ · J. S. Wróbel¹

Received: 4 January 2025 / Revised: 16 September 2025 / Accepted: 5 October 2025

© The Author(s) 2025

Abstract

In this paper, the effect of hafnium, titanium, and molybdenum addition on the microstructure and properties of the aluminide layers deposited by using a chemical vapor deposition process on IN 713C nickel superalloy substrate was discussed. A multi-component aluminide diffusion layer containing Ni–Al, Al–Ti–Ni, and hafnium-rich phases was successfully formed by aluminizing IN 713C nickel superalloy. Subsequently performed corrosion resistance tests confirmed the beneficial effect of the aluminide layer deposited on IN 713C as compared to substrate material. Anticipating improved mechanical response of coated material, density functional theory calculations were performed. It was found that a single Hf/Ti/Mo atom prefers to be positioned within the Al sublattice in the NiAl, and Ni₃Al phases. This justifies the presence of the experimentally observed Ni₃Hf phase in the Hf-enriched IN 713C. The Hf modification effects on the NiAl, and Ni₃Al were further discussed based on the changes of the elastic constants C_{ij} , bulk modulus B , and shear modulus G . The presence of Hf in NiAl causes a decrease of phase's C_{12} and C_{44} values, and increase in the C_{11} value. It was found that Hf modification of the Ni₃Al causes a decrease in the C_{ij} values and a slight decrease of phase's B/G ratio, indicating a less ductile character of modified phase decohesion.

Keywords IN 713C · CVD · Aluminide layer · Corrosion resistance · SEM · Ab initio calculations

1 Introduction

The IN 713C nickel-based superalloy was strategically selected for this study due to its widespread use in high-temperature, high-stress environments—particularly in the aerospace sector, where it is utilized for turbine blades, vanes, and rotors in jet engines [1–3]. This material offers a combination of superior casting properties, high-temperature oxidation resistance, and creep strength [1, 4], which are essential for maintaining structural integrity under extreme operating conditions such as those experienced in gas turbines, where combustion gases can reach temperatures up to 1650 °C [5]. However, despite its inherent advantages, IN 713C is still susceptible to electrochemical and hydrogen-induced corrosion, especially when exposed to aggressive environments involving moisture, sulfur compounds (e.g., Na₂SO₄), and prolonged low-frequency operation [6]. Such conditions accelerate intergranular cracking, reduce ductility, and compromise the service life of critical components. The decision



to further enhance IN 713C's corrosion and mechanical resistance using aluminide coatings via the chemical vapor deposition (CVD) method aligns with emerging surface engineering approaches aimed at extending the longevity of nickel superalloys under corrosive conditions. In particular, the introduction of hafnium, titanium, and molybdenum dopants is informed by prior evidence showing that these elements can influence phase stability and improve mechanical performance when introduced into Ni–Al intermetallic matrices. The suitability of IN 713C for such modifications is also supported by its well-documented behavior under high-temperature deformation, oxidation, and microstructural evolution, which provides a strong baseline for evaluating the effects of additional surface treatments.

Additionally, the literature supports the potential of aluminide coatings doped with various elements as promising candidates for research on advanced barrier coatings, further enhancing the corrosion resistance of nickel-based superalloys in demanding environments [7–10]. Electrochemical corrosion is the most critical factor affecting the durability and performance of these materials and numerous studies have examined the degradation of hot turbine components [11–18] and the effectiveness of protective surface treatments [19–24]. Low-temperature corrosion processes further shorten the service life of aircraft engines. At high temperatures, oxidation occurs due to sulfur from aviation fuel, leading to the development of microcracks. As a result, even protective surface coatings with hydrocarbons from technical oils cannot fully prevent electrochemical corrosion. Additionally, as an aircraft engine cools, moisture may form and, combined with unburnt fuel, can damage both the protective coating and the substrate material. Electrochemical corrosion is particularly harmful to aircraft engines operating at low frequency or those with extended periods of inactivity. Thus, oil-based surface protection becomes ineffective when foreign particles containing sulfur and hydrogen are present. Oxygen and hydrogen further accelerate corrosion, even when the surface is coated with oil or when foreign bodies detach, exposing the underlying material to the aggressive environment. It is worth emphasizing that hydrogen-induced damage is a well-known cause of failure in Inconel components. Hydrogen exposure leads to intracrystalline cracking in nickel and its alloys, reducing their plasticity. This phenomenon is commonly observed in modern nickel superalloys, such as the Ni–Cr–Fe type (IN 718) [25]. The extent of damage is influenced by the degree of hydrogen saturation along grain boundaries, which is directly related to the number of dislocations in the material that trap hydrogen [26]. Furthermore, an increase in dislocations, commonly occurring under high-temperature creep conditions [27], enhances hydrogen saturation, and accelerates the degradation of nickel-based alloys in hydrogen-rich environments. This saturation is influenced by factors such as hydrogen gas pressure, cathode potential, and the presence of hydrogen permeation promoters. Given the detrimental effects of low-temperature corrosion, improving the corrosion resistance of nickel alloys can be achieved through surface engineering techniques, such as applying protective layers using CVD methods [28, 29]. Existing studies have explored hydrogen's impact on the degradation of protective coatings [30, 31] and nickel alloys like IN 718 and IN 625 [32]. However, there is no literature available on the effect of hydrogen on the corrosion resistance of the IN 713C nickel alloy in its as-received state or with a protective coating.

To address the lack of data concerning the behavior of IN 713C nickel superalloy in hydrogen-rich corrosive environments—particularly with protective coatings—this study proposes the development of a novel Ni–Al-based surface layer modified with hafnium (Hf), titanium (Ti), and molybdenum (Mo). The application of CVD enables precise control over the composition and structure of the coating, facilitating the formation of a multi-component diffusion layer with potentially enhanced protective properties. This approach directly extends the findings from our prior work [6], in which aluminide layers enriched with zirconium (Zr) and chromium (Cr) were deposited on IN 713C substrates using the same CVD methodology. That study demonstrated that the incorporation of selected alloying elements into the aluminide layer can significantly alter its microstructure and improve its resistance to corrosion and mechanical degradation. However, the previous research focused primarily on the structural integrity and oxidation resistance of the Zr- and Cr-modified layers, without addressing the implications of hydrogen exposure—a critical factor in turbine engine applications where hydrogen embrittlement can compromise material reliability. In the present work, we build upon these foundational insights by introducing Hf, Ti, and Mo, which are known to influence phase stability, corrosion mechanisms, and hydrogen interactions

in nickel-based systems. Additionally, we integrate density functional theory (DFT) calculations to complement the experimental observations, offering atomic-scale insight into the substitution behavior, and mechanical consequences of these dopants within NiAl and Ni₃Al phases. By combining surface engineering with first-principles modeling, this study aims to provide a more comprehensive understanding of how multi-element aluminide coatings can be optimized for hydrogen-rich service environments. This dual experimental-computational approach marks a significant advancement over prior work and addresses an important gap in the literature regarding IN 713C alloy corrosion behavior under dual exposure to halides and hydrogen.

2 Research methodology

2.1 Materials and coating deposition details

Aluminide layers modified with Hf were deposited on a substrate of IN 713C nickel superalloy by using the CVD method. IN 713C is characterized by hardness of 358HV10, yield strength of 664 MPa, tensile strength of 819 MPa, elongation of 7.9% and Young modulus of 200 GPa [33]. The chemical composition of the superalloy is given in Table 1.

Prior to aluminization, the surfaces of the IN 713C nickel superalloy specimens were firstly ground using sandpaper, then activated by sandblasting and rinsed in acetone in an ultrasonic cleaner. The aluminization was carried out at a temperature of 1040 °C under a reduced pressure of 150 mbar, in two stages. The first stage consisted of 1 h of exposure to AlCl₃ in hydrogen. The modification of the aluminization process using hafnium involved the application of an additional external generator containing hafnium granules. The hafnium was activated by the flow of HCl and hydrogen. In the last stage, the outer zone of the layer was modified by hafnium vapors for 30 min only. The microstructures of the formed layers were observed using a Hitachi SU70 scanning electron microscope with SE and BSE detectors equipped with a Thermo Noran attachment for chemical composition analysis. To gain more information about the structure of the top layer, TEM observations were performed. The specimens were cut in cross-section from the layer zone and prepared using a Gatan commercial precision ion polishing system with a beam voltage of 4 V directed at an angle of 10° to the specimen surface. X-ray diffraction (XRD) measurements were executed at room temperature using a Bruker D8 Advance diffractometer with a Cu anode (Cu K α =0.154056 nm) and a parallel beam configuration operating at 40 kV and 40 mA, respectively. The measurements were made in an ($\omega - 2\theta$) setup with a constant ω angle of 2° between the direction of the incoming beam and the specimen surface. XRD diffraction patterns were recorded in a 2θ range of 20°–100°, with a step size of 0.05° and an acquisition time of 5 s. The XRD patterns were analyzed using Bruker EVA software and the PDF-2 database (from the International Centre for Diffraction Data).

2.2 Corrosion test

The corrosion resistance tests of IN 713C nickel superalloy in the initial state, with a CVD-produced aluminide layer, and after saturation with cathodic hydrogen were performed using the impedance (EIS) and potentiodynamic (LSV) methods on AutoLab PGTSTAT 100 potentiostat in a solution of 0.1 M NaCl + 0.1 M N₂SO₄ (pH 6.35) at room temperature (Fig. 1). Before the electrochemical examinations, the specimens were exposed to a corrosive solution under electroless conditions for the time required for their corrosion potential stabilization (about 1 h).

Table 1 Chemical composition of the IN 713C nickel superalloy

Element	Cr	Al	Ti	Nb	Mo	Fe	W	C	Ni
% mass	14.8	12.3	1.2	1.5	2.6	0.5	0.8	0.12	Bal.

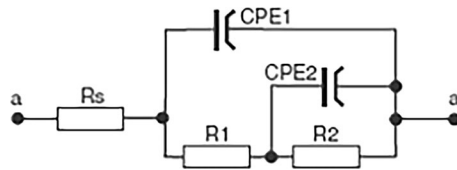


Fig. 1 Schematic diagram of the electrical equivalent circuit used in the tests. R_s environmental resistance, R_1 dielectric layer resistance/outer zone, R_2 double layer resistance (= charge transfer resistance through the double layer, CPE_1 dielectric layer capacitance, CPE_2 double layer capacitance)

The impedance tests were performed in a three-electrode system [test electrode—reference electrode (saturated SCE calomel electrode)—auxiliary electrode (platinum)] within a frequency range of 10^5 – 10^{-3} Hz, where the sinusoidal signal amplitude was equal to 10 mV at an open circuit potential. The impedance spectra were analyzed using the Baukamp EQUIVCRT program. To analyze the spectra obtained, an equivalent circuit was used having two $R(Q[R(RQ)])$ time constants as are commonly applied in electrochemical analyses of coatings [34]. The selection of equivalent circuit for the impedance spectra obtained was conditioned by the corrosion damage, the presence of the coating, and the slightest errors in matching the elements of the system (determined by the least squares method). The determined spectra were rendered in the form of Bode plots. Potentiodynamic tests were conducted in an identical three-electrode system at a potential of 1000 mV. The material was polarized at a potential change rate of 0.2 mV/s. IN 713C, both in the initial state and with a CVD-produced aluminide layer, were saturated with hydrogen using the cathodic hydrogen charging (50 mA/cm^2 , 6 h, room temperature) to induce accelerated hydrogen degradation. A solution of 0.5 M H_2SO_4 with the addition of $1 \text{ mg/dm}^3 \text{ As}_2\text{O}_3$ was used to promote hydrogen permeation.

2.3 DFT calculations

DFT calculations were executed using the Vienna Ab initio Simulation Package (VASP) [35, 36]. Cutoff energy equal to 400 eV, and the Monkhorst–Pack mesh [37] of k points in the Brillouin zone, with a k -mesh spacing of 0.15 \AA^{-1} was used. To evaluate the impact of the alloying additives on the electronic and mechanical properties of the NiAl, its $2 \times 2 \times 2$ supercells with 16 atomic sites were constructed, with a single Ni or Al atom replaced with an Hf/Ti/Mo atom. This resulted in a substituent concentration of 6.25 at.%. The FCC-based structures were generated analogously, resulting in a 3.125 at.% concentration of Hf/Ti/Mo. All DFT calculations were performed with collinear spin-polarization.

To determine the energetically preferred position of Hf/Ti/Mo in the NiAl and Ni_3Al phases, the structures were subjected to full cell relaxation with force components relaxed to 10^{-4} eV/\AA , and the total energies were converged to 10^{-5} eV . Two possible nodal positions (Ni and Al sublattices) were examined for each substituent. Based on the calculated energies of the examined structures, the defect formation energy E_f was established, using the equation [38]:

$$E_f = E_{\text{modified}} - E_{\text{perfect}} \pm \sum_i \mu_i,$$

where E_{modified} , E_{perfect} , μ_i are the energy of the modified intermetallic structure (with the added atom), the energy of pure (unmodified) NiAl or Ni_3Al phase, and the chemical potential of the added Hf/Ti/Mo (–) or removed Ni/Al (+) atom, respectively. In this work, μ_i of Ni and Al was calculated separately for NiAl, and Ni_3Al , using Widom-type substitution [39]. Because of the high computational cost, the μ_i of Hf/Ti/Mo was assumed to be equal to the energy per atom in each element's ground state. Such simplification does not influence the determination of preferable substitute positioning and provides accurate results for the purpose of this study.

After the determination of the preferred substitute positioning, the elastic properties of the relaxed structures were computed using a finite differences approach, with ions being displaced in each direction by positive and

negative displacement. The width of subsequent displacements of each ion was equal to 0.015 Å. Obtained matrix of elastic constants C_{ij} was used to calculate bulk modulus B and shear modulus G , according to the equations:

$$B = \frac{C_{11} + 2C_{12}}{3}$$

$$G_V = \frac{C_{11} - C_{12} + 3C_{44}}{5}$$

$$G_R = \frac{5[(C_{11} - C_{12}) \times C_{44}]}{[4C_{44} + 3(C_{11} - C_{12})]}$$

$$G = G_{VRH} = \frac{G_V + G_R}{2},$$

where subindexes: V, R, and V-R-H denote the Voigt, Reuss, and Hill averaging procedures, respectively [40–42]. The values of B and G were then used to determine the plasticity of the materials using the Pugh plasticity criterion B/G [43].

3 Experimental results

3.1 Characteristics of the layers

The morphology of the aluminide layer formed on the substrate of nickel alloy IN 713C after CVD process was shown in Fig. 2a. The surface image of the layer obtained using SEM in backscattered electron (BSE) contrast suggests a multi-component structure. Fine particles and bright-colored microareas, well integrated into the surface of the dark-colored region are observed. Chemical composition analysis performed using energy dispersive spectroscopy (EDS) in microareas revealed that the bright areas predominantly contain hafnium at approximately 70% by mass.

Conversely, the dark areas predominantly contain nickel at 82% by mass, aluminum at 10.8% by mass, and lower amounts of titanium, niobium, and chromium. The cross-section of the layer is presented in Fig. 2b. The visible grains are defective and exhibit a columnar-like structure. The formed layer, approximately 8 μm thick, exhibits a complex structure. The outer zone of the layer, approximately 2–3 μm thick, is homogeneous. Below this zone, a darker, aluminum-rich zone with fine hafnium precipitates is visible. The multi-component structure of the layer could be clearly observed based on elemental distribution maps (Fig. 2c).

The maps presented in Fig. 2c depicting the distribution of elements in the cross-section of the layer confirm the presence of hafnium islets on the layer surface. The absence of a continuous zone on the layer’s surface is likely caused by the relatively short introduction time (30 min) of hafnium alone into the layer. These distribution maps indicate that the outer zone of the layer is relatively homogeneous, containing a constant and relatively high nickel content compared to aluminum, suggesting that the phases present in this zone are nickel-rich.

The analyzed outer zone of the layer presented in Fig. 2 differs significantly in aluminum concentration from the aluminide layer produced using the CVD method in the works [44, 45], where the outer zones of the studied aluminide layers were much richer in aluminum. Since different materials were used as substrates in the cited works and significantly longer aluminization process time were used, it is difficult to clearly state that in the last phase of aluminization, lasting stage of 30 min, the process of introducing hafnium into the layer itself reduced the aluminum content in its outer zone. Therefore, in the further part of the work, DFT calculations were carried out to explain how adding hafnium affects the phase composition of the intermetallic layer formed from the Ni–Al

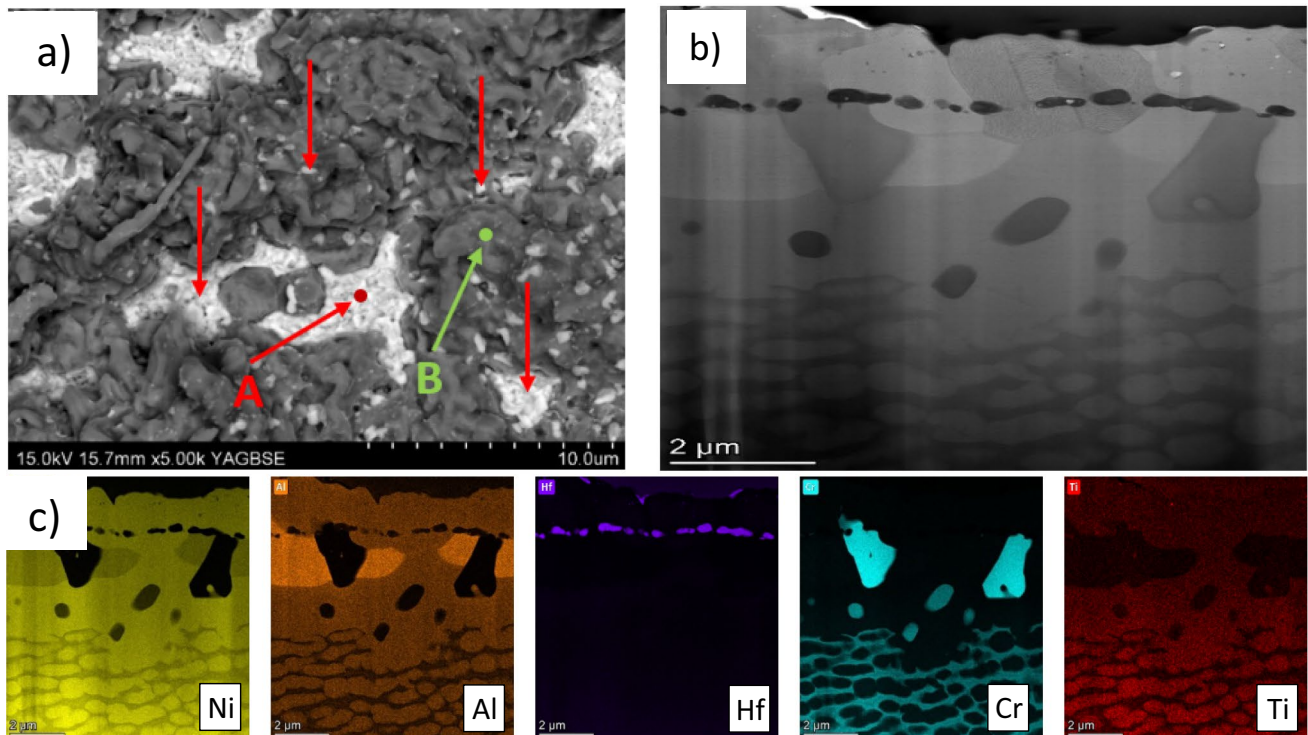


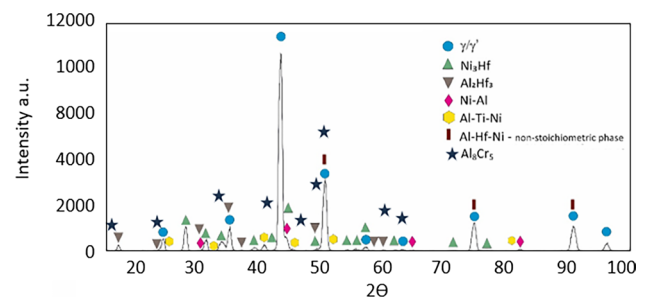
Fig. 2 Morphology (a), spectrograms from surface (b) and cross-section of the aluminide layer produced on IN 713C through CVD method with distribution of the chemical elements (c)

system. Below this zone, there is an increased concentration of aluminum and fine hafnium precipitates (Fig. 2). The microareas rich in chromium observed in the inner sub-layer are due to the low solubility of this element (approximately 10 at.% at a temperature of 1423 K) in the β -NiAl intermetallic phase [46] and the diffusion of nickel towards the surface.

3.2 Phase composition analysis

X-ray diffraction (XRD) was employed to analyze the phase composition of the layer (Fig. 3). Since the experiment was conducted with a constant primary beam angle of 2° , the X-rays penetrated and interacted with the material's crystal lattice in a minimal volume, compared to the Bragg–Brentano configuration. The results revealed a range of intensity peaks, including reflections from the substrate material, specifically the (γ) matrix and the phase reinforcing the IN 713C alloy— γ' . The layer's characteristic structure, as shown in Fig. 3, is typical of aluminized layers, further confirming the diffusive nature of the applied process. This diffusion affects the diffraction

Fig. 3 X-ray diffractogram with phase analysis obtained from a layer created in an aluminization process modified with hafnium



pattern, where the chemical composition of the identified phases is often non-stoichiometric. The diffraction peaks were observed to be asymmetric, indicating the co-existence of multiple phases in the same region. This phase overlap, combined with the non-stoichiometric nature of the composition, complicates the analysis and precise attribution of peaks to specific phases. Nevertheless, the presence of intermetallic phases from the Ni–Al and Al–Ti–Ni systems, as well as hafnium-containing phases such as Ni₃Hf (hexagonal structure, Space Group 136: P42/mnm), Al₂Hf₃ (tetragonal structure, Space Group 194: P63/mmc), and a non-stoichiometric Al–Hf–Ni phase, was confirmed. The peak positions also suggest that the chromium-rich precipitates seen in Fig. 2 may form the intermetallic phase Al₈Cr₅ (trigonal crystal system, Space Group R3m: R). In conclusion, the deposition process was successfully applied, and the layer's effectiveness was further validated through corrosion resistance testing.

To deepen the insight into the complex phase composition of the aluminide layer, a quantitative phase analysis (QPA) was carried out using Rietveld refinement of the X-ray diffraction (XRD) patterns. The refinement was performed using the Bruker TOPAS software package. A pseudo-Voigt function was employed to fit the diffraction profiles, with the background modeled using a Chebyshev polynomial. Instrumental broadening was calibrated using a LaB₆ standard. The refinement parameters included lattice constants, phase scale factors, and profile shape parameters. The crystalline phases identified in the qualitative XRD analysis (NiAl, Ni₃Hf, Al–Ti–Ni, Al₂Hf₃, and Al₈Cr₅) were used as input structural models. The Rietveld analysis yielded a good agreement between the measured and calculated diffraction patterns ($R_{wp} < 10\%$), confirming the presence of a multi-phase structure in the surface-modified layer. The estimated weight fractions of the detected crystalline phases are summarized as follows: NiAl (~36 wt%), Ni₃Hf (~27 wt%), Al–Ti–Ni ternary phase (~16 wt%), Al₂Hf₃ (~12 wt%), and Al₈Cr₅ (~6 wt%), with the remaining fraction attributed to residual γ/γ' matrix components from the substrate. These results correlate well with the SEM/EDS data, which showed Ni- and Hf-rich regions interspersed within the aluminide matrix. The predominance of NiAl and Ni₃Hf is consistent with the thermodynamic stability of these phases at the aluminization temperature (1040 °C) and supports the DFT results indicating a strong energetic preference for Hf substitution into the Al sublattice of NiAl and Ni₃Al. This substitution mechanism contributes to the stabilization of the Ni₃Hf phase, which likely forms via local compositional enrichment during the post-aluminization hafnium exposure. The Al–Ti–Ni phase presence, although less pronounced, reflects partial incorporation of Ti from the base alloy or vapor phase, forming a solid solution with NiAl under CVD conditions. Similarly, the Al₂Hf₃ phase—an Hf-rich intermetallic compound—accounts for the bright islets observed in BSE micrographs and the localized hafnium enrichment confirmed by EDS. Interestingly, the presence of the Al₈Cr₅ phase, albeit in a small fraction, is indicative of chromium segregation during diffusion and its low solubility in the NiAl matrix. This finding aligns with the elemental maps showing Cr enrichment near the inner sublayer and may point to early-stage spinodal decomposition or precipitation hardening phenomena. Quantifying these phases allows for a more nuanced understanding of the layer's mechanical and electrochemical performance. For example, the significant fraction of Ni₃Hf—a phase with higher hardness but lower ductility than Ni₃Al—explains the slightly reduced B/G ratio obtained from DFT calculations. Likewise, the formation of multiple intermetallics with varying electrochemical activity contributes to the observed heterogeneity in impedance spectra, particularly under hydrogen exposure.

3.3 Corrosion resistance tests

The results of the corrosion resistance tests performed on IN 713C nickel superalloy in the initial state (IS) and with an aluminide layer are presented in Fig. 4a and c. The impedance spectra after cathodic hydrogenation are presented in Fig. 4b and d. In all cases, the presence of two time constants is observed, indicating two electrochemical processes taking place on the material surface.

In the initial material, the presence of two time constants is caused by high microstructural heterogeneity, in which equiaxed grains of dendrite cores and inter-dendritic areas can be distinguished. Dendritic structures consist of γ' precipitates surrounded by matrix channels, while the enrichment of inter-dendritic spaces with carbide-forming elements may lead to the production of, among others, γ/γ' eutectics or MC-type carbides

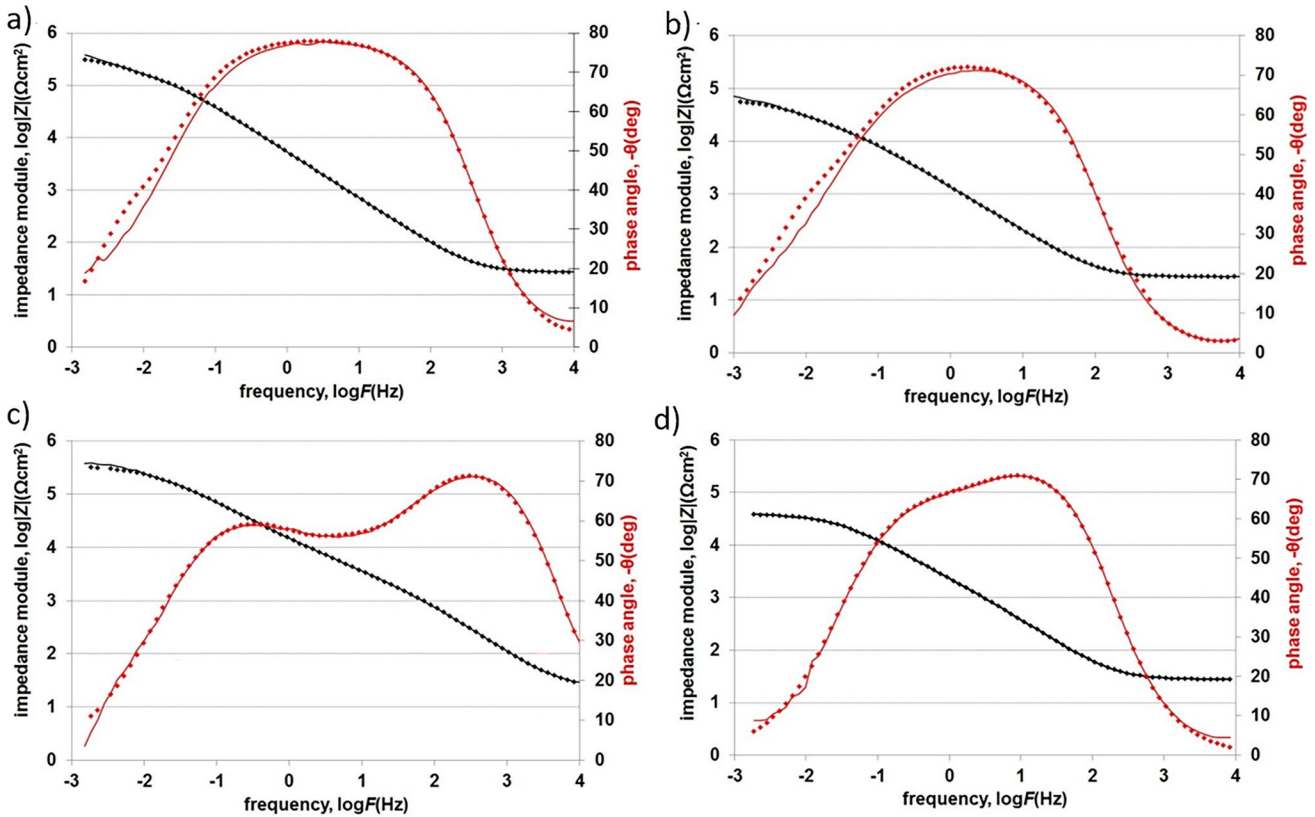


Fig. 4 Impedance spectra of IN713C nickel superalloy in the initial state (a), with an aluminide layer (c), and after cathodic hydrogenation (b, d). Solid line—data, dotted line—fitting

enriched in Nb [6]. It can be assumed that the observed two capacitive peaks with significant coincidence describe the electrochemical parameters of the dendrite zone and inter-dendritic areas. The ‘*n*’ parameter of the analyzed areas indicates the presence of passive areas ($n = 1$) surrounded by passive-active areas ($n = 0.88$). The aluminization process significantly increased the corrosion resistance of the material with a notable increase in the electrochemical heterogeneity of the substrate (Fig. 5). The resistance to charge transfer through the double layer (resistance R_t) increased from 88 to 366k $\Omega \text{ cm}^2$. This is evidenced by the presence of a clearly marked additional capacitive peak occurring in the low-frequency range. The ‘*n*’ parameter of the produced dielectric layer (Table 2) is typical for passive-active metallic layers subjected to local corrosion. It can be assumed that the places initiating corrosion are areas enriched in hafnium compounds (increasing

Fig. 5 Potentiodynamic curves of IN 713C nickel superalloy: in the initial state before (A) and (B) after cathodic hydrogenation, with aluminide layer before (C) and after cathodic hydrogenation (D)

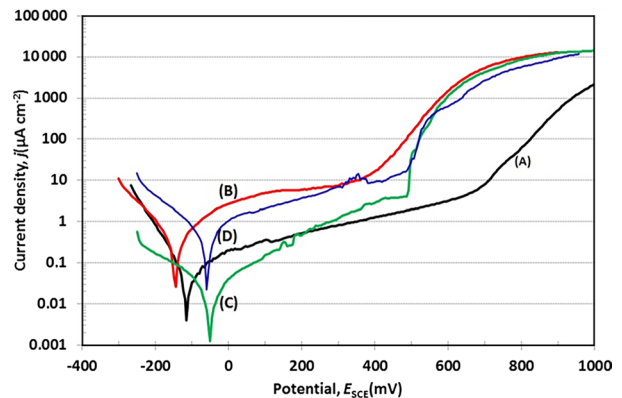


Table 2 Summary of results of the electrochemical corrosion tests (impedance tests)

		Dielectric layer	Error* (%)	Outer zone	Error* (%)	Electric double layer	Error* (%)
IN 713C in initial state	R (Ωcm^2)			1.99×10^5	5.5	8.82×10^4	23.2
	Y_{OCPE} ($\text{F}/\text{cm}^2 \times \text{s}^{n-1}$)			3.67×10^{-5}	0.9	2.42×10^{-4}	66.3
	N			0.88	0.2	1	15.5
IN 713C in initial state and after hydrogenation	R (Ωcm^2)			2.98×10^4	14.1	3.25×10^4	20.8
	Y_{OCPE} ($\text{F}/\text{cm}^2 \times \text{s}^{n-1}$)			1.55×10^{-4}	2.2	3.78×10^{-4}	61.0
	N			0.84	0.7	0.82	16.3
IN 713C with aluminate layer	R (Ωcm^2)	4.70×10^3	6.2			3.66×10^5	1.8
	Y_{OCPE} ($\text{F}/\text{cm}^2 \times \text{s}^{n-1}$)	4.61×10^{-6}	4.3			1.41×10^{-5}	1.5
	N	0.87	0.6			0.71	0.8
IN 713C with aluminate layer after hydrogenation	R (Ωcm^2)	4.11×10^3	10.6			3.60×10^4	1.7
	Y_{OCPE} ($\text{F}/\text{cm}^2 \times \text{s}^{n-1}$)	6.74×10^{-5}	2.0			4.77×10^{-5}	2.4
	N	0.88	0.4			0.71	1.4

R resistance, Y_{OCPE} capacity of constant phase element, n coefficient of imperfections of constant phase element (CPE); an empirical constant ranging from 0 to 1. It is worth noting that when $n=1$, the CPE behaves as a pure capacitor, while when $n=0$, the CPE behaves as a pure resistor

*Error (%)—sum of squares of deviations between measured data points and the calculation line

Table 3 Summary of results of the electrochemical corrosion tests (potentiodynamic tests)

	E_{ocp} (mV _{SCE})	E_{corr} (mV _{SCE})	E_{np} (mV _{SCE})	I_{corr} ($\mu\text{A}/\text{cm}^2$)
IN 713C (initial state)	- 90	- 115	660	5.1×10^{-2}
IN 713C (initial state after hydrogenation)	- 130	- 145	390	34×10^{-2}
IN 713C with an aluminide layer	- 65	- 50	480	2.3×10^{-2}
IN 713C with an aluminide layer after hydrogenation	- 40	- 60	470	41×10^{-2}

E_{ocp} , open circuit potential; E_{corr} , corrosion potential; I_{corr} , corrosion current density; E_{np} , breakdown potential

the local dielectric permittivity) or a cavity in the rough aluminide layer. In these places, there are conditions favorable for corrosion of the metallic electrode ($n = 0.70$).

On the other hand, the cathodic hydrogen saturation process (50 mA/cm²/6 h) reduced the corrosion resistance in both analyzed cases. The charge transfer resistance through the double layer (R_t) of the IN 713C nickel superalloy in the initial state decreased from 88 to 32k Ωcm^2 , and in the case of the dielectric layer from 366 up to 36k Ωcm^2 .

The presence of dissolved hydrogen in the nickel alloy resulted in a deterioration of its mechanical properties through loss of ductility and tensile strength. The formed aluminide layer did not protect the substrate against the unfavorable effects of hydrogen, as evidenced by a decrease in the value of the charge transfer resistance through the double layer and a negative change in the values of the electrochemical parameters of the dielectric layer. An increase in the capacitance of the dielectric layer indicates a decrease in its thickness.

Figure 5 shows the potentiodynamic curves of the tested materials. In the case of an aluminide coating, due to the presence of hafnium in the coating, which has a strong affinity for oxygen [47], a shift of corrosion potentials towards the anodic side was observed. On the other hand, the presence of Al and Ti compounds enhances the corrosion resistance of the substrate. Additionally, the presence of hafnium oxide may undergo intense electrochemical corrosion in acidic and alkaline environments due to its amphoteric nature. In the case of neutral solutions, precipitates rich in Hf (due to their low electronegativity of $E = 1.3$) may react with other elements of the coating creating microcells inducing galvanic corrosion, thus reducing the durability of the aluminide layer. The reduction in the passive range ($\Delta E_{np} = -180$ mV) is caused by both a significant increase in the roughness of the aluminide layer as well as the presence of a passive layer of hafnium oxides, which in the presence of halide ions (Cl^- , F^- , Br^-) is susceptible to pitting corrosion. The obtained results, presented in Table 3, are consistent with literature data [48] indicating the negative impact of Hf on the corrosion resistance of nickel-based alloys. The results presented confirm the adverse impact of cathodic hydrogenation on both the IN 713C nickel alloy in the initial state and on the quality of the aluminide layer produced by using CVD. It was deduced, that one of the factors determining the detrimental effect of hydrogenation on the quality of the layer is the type of crystal lattice [31]. With the connections of the same type of crystal cell of similar diffusion and hydrogen solubility coefficients, the aluminide layer exhibits better performance in an environment containing hydrogen. However, if the crystallographic cells differ, the adverse impact of the presence of hydrogen occurs. The absorption of hydrogen by hafnium to form ternary hydride is a commonly observed phenomenon, and their presence negatively affects the mechanical and electrochemical properties of nickel alloys.

Although the addition of hafnium was not successful in terms of enhancement of corrosion resistance, the presence of Al and Ti compounds in the coating improved the corrosion resistance of the substrate. Therefore, it was concluded, that CVD could be recommended as an additional surface treatment process that increases the corrosion resistance of IN 713C alloy. Since beneficial effects of CVD application for material protection were confirmed, further analysis of substrate material with layer was performed with special emphasis on its mechanical response as compared to its as-received state.

The corrosion mechanism of the IN 713C nickel superalloy, particularly after modification with a hafnium-doped aluminide layer, involves multiple complex interactions at the microstructural and electrochemical levels.

In its native state, IN 713C is vulnerable to electrochemical corrosion due to the heterogeneous nature of its dendritic structure, which fosters galvanic coupling between γ/γ' phases and carbides. The introduction of Cl^- and SO_4^{2-} anions in the corrosive medium promotes the breakdown of passive films, accelerating localized corrosion. Upon deposition of the aluminide layer, a protective barrier composed predominantly of Ni–Al intermetallics and Hf-rich phases is established. These phases initially enhance resistance by providing a diffusion barrier to oxygen and corrosive species. However, due to the amphoteric nature of HfO_2 , its stability in neutral or halide-rich environments is compromised. The presence of hafnium can form galvanic couples with surrounding Ni–Al or Al–Ti–Ni intermetallics, acting as cathodic sites and initiating pitting corrosion. Moreover, cathodic hydrogen charging results in the absorption of hydrogen into both the substrate and the coating. Hf, being a strong hydrogen getter, contributes to the formation of brittle hydride phases (e.g., HfH_2), which act as crack initiation sites and degrade mechanical integrity. This is consistent with known embrittlement mechanisms in Ni-based superalloys, where hydrogen accumulates at grain boundaries and dislocation cores, facilitating intergranular fracture. The heterogeneity introduced by hafnium-containing inclusions exacerbates this process, leading to early decohesion and reduced corrosion resistance.

The present study demonstrates that the deposition of an Hf-doped aluminide layer via the CVD method substantially modifies both the microstructure and corrosion performance of the IN 713C nickel superalloy. The formation of distinct phases such as Ni_3Hf , Al_2Hf_3 , and non-stoichiometric Al–Hf–Ni compounds in the outermost layer reflects the incorporation of Hf primarily in the Al sublattice of the NiAl and Ni_3Al phases, as confirmed by DFT calculations. The mechanical implications of these substitutions are notable. The DFT results suggest that Hf doping marginally reduces the *B/G* ratio in Ni_3Al , implying a more brittle decohesion mode. Conversely, Mo doping was found to enhance plasticity by significantly increasing the *B/G* ratio. From a mechanical perspective, these changes suggest trade-offs between corrosion performance and mechanical robustness, which must be carefully balanced for aerospace applications. Similar conclusions can be drawn for materials joined using welding techniques, where the optimization of properties between corrosion resistance and mechanical strength is crucial [49, 50]. Electrochemical measurements indicate that while the aluminide coating enhances the initial corrosion resistance by forming a diffusion barrier and stabilizing the passive film, its performance degrades significantly under hydrogenating conditions. The drop in charge transfer resistance and the emergence of more capacitive behavior suggest hydrogen permeation and subsequent breakdown of the passive layer. The localized increase in dielectric constant near Hf-rich inclusions supports the notion of galvanic interactions and pitting initiation in these areas. This aligns with studies highlighting the amphoteric and reactive nature of hafnium oxides in neutral to mildly acidic media. Importantly, while the presence of Hf was not universally beneficial for corrosion resistance—particularly in hydrogen-rich environments—it did contribute to the formation of phases with potentially favorable high-temperature oxidation behavior. Therefore, the selection of dopants in aluminide coatings should

Table 4 Summary of calculations using the DFT method of the defect formation energy (E_f) in systems with Hf/Ti/Mo substitution (preferred substitutions marked in bold)

Base structure	Compound	E_f (eV)
NiAl	Ni_7HfAl_8	– 5.486
	$\text{Ni}_8\text{Al}_7\text{Hf}$	– 11.280
	Ni_7TiAl_8	– 2.029
	$\text{Ni}_8\text{Al}_7\text{Ti}$	– 7.095
	Ni_7MoAl_8	– 8.435
	$\text{Ni}_8\text{Al}_7\text{Mo}$	– 11.757
Ni_3Al	$\text{Ni}_{23}\text{HfAl}_8$	– 8.820
	$\text{Ni}_{24}\text{Al}_7\text{Hf}$	– 11.255
	$\text{Ni}_{23}\text{TiAl}_8$	– 4.827
	$\text{Ni}_{24}\text{Al}_7\text{Ti}$	– 6.806
	$\text{Ni}_{23}\text{MoAl}_8$	– 9.656
	$\text{Ni}_{24}\text{Al}_7\text{Mo}$	– 11.954

Table 5 Summary of elastic properties calculated using the DFT method for the perfect structures of NiAl and Ni₃Al

Property	NiAl	NiAl (exp.) [48]	NiAl (DFT-literature) [31, 49]	Ni ₃ Al	Ni ₃ Al (exp.) [50, 51]	Ni ₃ Al (DFT-literature) [50, 52]
C_{11}	198	199	209, 200	246	230, 221	230, 228
C_{12}	140	137	135, 131	151	150, 146	139, 160
C_{44}	118	116	118, 117	131	131, 124	123, 124
B	159	156	160, 154	183	177, 171	169, 171
G	68		74, 68	87	82, 77	83, 74
B/G	2.35		2.16, 2.26	2.10	2.17, 2.22	2.05, 2.48

C_{ij} , B , and G values are expressed in GPa

Properties derived from our own research are in bold, while literature data are in normal font. However, if this is unnecessary, please request a font change

consider both their thermodynamic site preferences and their chemical reactivity under service-specific conditions. Future work could explore ternary or quaternary modifications, possibly integrating rare earth or noble metals to stabilize the passive layer while mitigating the galvanic effects introduced by Hf.

3.4 DFT calculations

The calculated E_f values of Hf/Ti/Mo substitution in the NiAl and Ni₃Al phases are given in Table 4. Negative E_f means that the formation of a defect is energetically favorable, and vice versa. The lower E_f , the more stable the structure is. Based on the results presented in Table 4, one can conclude that Hf, Ti, and Mo preferably occupy the Al position in both investigated intermetallic phases. This is in agreement with other ab initio studies of NiAl [51], and Ni₃Al [52] phases. The DFT-determined site preference of Hf can explain the phase composition of the experimentally manufactured alloy, described in the previous Sections. As visible in Fig. 3, the Hf enrichment of IN 713C led to the Ni₃Hf phase formation. Interestingly, this phase has the same stoichiometry as the Ni₃Al present in the unmodified alloy. Those observations can lead to the conclusion that the Ni₃Hf phase may be a result of the substitution of Al atoms by Hf in the Ni₃Al phase.

In the next step, the elastic constants of the NiAl and Ni₃Al single crystals were calculated. The results are presented in Table 5. A comparison between the current DFT results, the experimental data, and the DFT calculations performed by other authors exposes excellent agreement. To keep the clarity of presentation, only some literature data was compared [53–56].

Subsequently, the corresponding elastic properties of the most stable (with the lowest E_f) substitutions were calculated, namely, those were the NiAl-based bcc structures Ni₈Al₇Hf, Ni₈Al₇Ti, Ni₈Al₇Mo, and the Ni₃Al-based fcc Ni₂₄Al₇Hf, Ni₂₄Al₇Ti, Ni₂₄Al₇Mo. The results for the substituted alloys are given in Table 5. The components of the C_{11} , and C_{44} elastic constant matrix calculated for Ni₂₄Al₇Hf are in very good agreement with the DFT

Table 6 Summary of the elastic properties calculated using the DFT method for systems with Hf/Ti/Mo substitution in the preferred positions of the crystal lattice for NiAl- and Ni₃Al-based structures

	NiAl-based			Ni ₃ Al-based			
	Ni ₈ Al ₇ Hf	Ni ₈ Al ₇ Ti	Ni ₈ Al ₇ Mo	Ni ₂₄ Al ₇ Hf	Ni ₂₄ Al ₇ Hf [53]	Ni ₂₄ Al ₇ Ti	Ni ₂₄ Al ₇ Mo
C_{11}	216	197	187	236	244	250	244
C_{12}	131	137	156	137	158	152	151
C_{44}	103	109	106	125	122	129	131
B	159	157	167	170	187	185	182
G	72	65	50	86	80	88	86
B/G	2.21	2.41	3.31	1.97	2.32	2.11	2.11

C_{ij} , B and G values are expressed in GPa

computation performed independently by Kim et al. [57]. While comparing the effect of examined substitutions on NiAl- and Ni₃Al-based structures, one can conclude that neither of those compounds is more prone to undergo significant changes in their elastic properties. The relative changes of the C_{ij} values in both intermetallic phases have a similar range of magnitudes. However, each Hf/Ti/Mo-substituted structure has different characteristics. One should observe, an increase in the C_{11} value for the Ni₈Al₇Hf structure, accompanied by a decrease in the C_{12} and C_{44} values. On the other hand, the Mo-modified NiAl structure had a higher C_{12} value, while the C_{11} and C_{44} values decreased, in comparison with the perfect NiAl phase. The substitution of Ti practically did not change the C_{11} and C_{12} values, while the C_{44} value exhibited the most significant decrease.

The comparison of the Hf-substituted structure with the perfect Ni₃Al data (Table 6), exposed that Hf substitution had a negligible impact on the elastic constants of this intermetallic phase, resulting in a slight decrease of its C_{ij} values. On the other hand, the presence of Ti and Mo did not affect the elastic properties of the phase notably. The highest changes of the bulk modulus B were observed for Mo substitution in NiAl phase and Hf-modified Ni₃Al. Moreover, the addition of Mo to the NiAl structure significantly affected the shear modulus G of the structure. The significant decrease of G value means lower resistance of the Mo-modified NiAl phase to deformation under the shear stress. These observations suggest that the Hf alloy doping may affect its ductility, which was further verified by evaluating the Pugh plasticity criterion expressed as the B/G ratio [43]. This criterion can be used to anticipate the plasticity of ceramics, intermetallic phases, and metals. The B/G ratio (where B is the strength of the chemical bonds and G is their resistance to shear without elongation) defines the susceptibility of a material to dislocation generation. A low B/G value means that the structure undergoes decohesion before the required strain is achieved, whereas a high value indicates that the material can be plastically deformed. The critical B/G value, below which a material undergoes brittle fracture, is about 1.75. Above such value, it may undergo plastic deformation. Therefore, the higher the B/G ratio, the more ductile the material is.

In all of the examined structures, the B/G ratio was higher than 1.75, meaning that those phases might undergo plastic deformation. In the case of the Mo-modified NiAl structure, the most significant change represented by 41% increase in the B/G ratio was observed. Therefore, the addition of Mo to NiAl results in a significant increase in phase's plasticity. Furthermore, the substitution of Hf in the NiAl, and Ni₃Al resulted in a slight decrease in their B/G ratio, meaning less ductile character at the decohesion of the modified alloy.

4 Conclusions

Based on the research conducted, the following conclusions can be formulated:

1. The corrosion resistance tests confirmed the beneficial effect of the aluminide layer on the corrosion resistance enhancement of the IN 713C nickel superalloy substrate. It was also found that the process of hydrogenation degraded the aluminide layer and significantly reduced the corrosion resistance of the IN 713C substrate.
2. The comparison of the defect formation energies revealed that a single Hf/Ti/Mo atom prefers to occupy the Al sublattice in the NiAl, and Ni₃Al phases. This result justifies the presence of the Ni₃Hf phase in the experimentally manufactured Hf-enriched IN 713C. The energetically stable Hf/Ti/Mo-doped NiAl and Ni₃Al structures had altered elastic properties from the perfect intermetallics. Hf enrichment of NiAl results in the decrease of phase's C_{12} and C_{44} values, and an increase in the C_{11} value. For the Ni₃Al phase, the Hf doping results in the C_{ij} value decrease, and a slight decrease of phase's B/G ratio. Based on that one can conclude that the Hf-enriched alloy surface may be more susceptible for the brittle decohesion, than the unmodified IN 713C.

Acknowledgements The DFT simulations were carried out with the support of the Interdisciplinary Centre for Mathematical and Computational Modelling (ICM), University of Warsaw, under Grant No. GB79-6. A.W. is grateful for the support from the European Union Horizon 2020 research and innovation program under Grant Agreement No. 857470 and from

the European Regional Development Fund under the program of the Foundation for Polish Science International Research Agenda PLUS, Grant No. MAB PLUS/2018/8, and the initiative of the Ministry of Science and Higher Education ‘Support for the activities of Centers of Excellence established in Poland under the Horizon 2020 program’ under agreement No. MEiN/2023/DIR/3795.

Funding This study was financed by the Warsaw University of Technology, Faculty of Materials Science and Engineering, from the statutory work 504/04812/1090/44.000000.

Data availability All data generated or analyzed during this study will be made available by the corresponding author to the editor, reviewers or researchers upon request and will be sent to the designated person.

Declarations

Conflict of interest All the authors declare that there is no conflict of interest.

Informed consent No animal or human subjects/participants were involved in the creation of the article.

Open Access This article is licensed under a Creative Commons Attribution 4.0 International License, which permits use, sharing, adaptation, distribution and reproduction in any medium or format, as long as you give appropriate credit to the original author(s) and the source, provide a link to the Creative Commons licence, and indicate if changes were made. The images or other third party material in this article are included in the article’s Creative Commons licence, unless indicated otherwise in a credit line to the material. If material is not included in the article’s Creative Commons licence and your intended use is not permitted by statutory regulation or exceeds the permitted use, you will need to obtain permission directly from the copyright holder. To view a copy of this licence, visit <http://creativecommons.org/licenses/by/4.0/>.

References


1. Coleman M, Alshehri H, Banik R, Harrison W, Biroscas S. Deformation mechanisms of IN713C nickel based superalloy during small punch testing. *Mater Sci Eng A*. 2016;650:422–31. <https://doi.org/10.1016/j.msea.2015.10.056>.
2. Keshavarz MK, Turenne S, Bonakdar A. Solidification behavior of inconel 713LC gas turbine blades during electron beam welding. *J Manuf Process*. 2018;31:232–9. <https://doi.org/10.1016/j.jmapro.2017.11.021>.
3. Łyczkowska K, Adamiec J. Repair of precision castings made of the Inconel 713C alloy. *Arch Foundry Eng*. 2017;17(3):210–6. <https://doi.org/10.1515/afe-2017-0117>.
4. Matysiak H, Zagorska M, Balkowiec A, Adamczyk-Cieslak B, Cygan R, Cwajna J, Nawrocki J, Kurzydłowski KJ. The microstructure degradation of the IN 713C nickel-based superalloy after the stress rupture tests. *JMEPEG*. 2014;23:3305–13. <https://doi.org/10.1007/s11665-014-1123-4>.
5. Raj R, Moskowitz S. Transpiration air protected turbine blades—an effective concept to achieve high temperature and erosion resistance for gas turbines operating in an aggressive environment. *78-GT-100*, Am Soc Mech Eng. 1978;(780):1–11.
6. Sitek R, Kwaśniak P, Sopicka-Lizer M, Borysiuk J, Kamiński J, Mizera J, Kurzydłowski KJ. Experimental and ab-initio study of the Zr- and Cr-enriched aluminide layer produced on an IN 713C Inconel substrate by CVD; investigations of the layer morphology, structural stability, mechanical properties, and corrosion resistance. *Intermetallics*. 2016;74:15–24. <https://doi.org/10.1016/j.intermet.2016.04.003>.
7. Thakare JG, Pandey C, Mahapatra MM, et al. Thermal barrier coatings—a state of the art review. *Met Mater Int*. 2021;27:1947–68. <https://doi.org/10.1007/s12540-020-00705-w>.
8. Thakare JG, Pandey C, Mulik RS, Mahapatra MM. Mechanical property evaluation of carbon nanotubes reinforced plasma sprayed YSZ-alumina composite coating. *Ceram Int*. 2018;44(6):6980–9. <https://doi.org/10.1016/j.ceramint.2018.01.131>.
9. Barwińska I, Kopeć M, Kukla D, Senderowski C, Kowalewski ZL. Thermal barrier coatings for high-temperature performance of nickel-based superalloys: a synthetic review. *Coatings*. 2023;13(4):1–21. <https://doi.org/10.3390/coatings13040769>.
10. Kopeć M. Recent advances in the deposition of aluminide coatings on nickel-based superalloys: a synthetic review (2019–2023). *Coatings*. 2024;14(630):1–15. <https://doi.org/10.3390/coatings14050630>.
11. Szczepankowski A, Przysowa R. Thermal degradation of turbine components in a military turbofan. *Eng Fail Anal*. 2022;134:106088. <https://doi.org/10.1016/j.engfailanal.2022.106088>.

12. Łyczkowska K, Adamiec J. The phenomena and criteria determining the cracking susceptibility of repair padding welds of the Inconel 713C nickel alloy. *Materials*. 2022;15(634):1–20. <https://doi.org/10.3390/ma15020634>.
13. Pauzi AA, Berahim N, Husin S. Degradation of gas turbine blades for a thermal power plant. *MATEC Web Conf*. 2016;54(303002):1–4. doi: 10.1051/mateconf/20165403002
14. Mevissen F, Meo M. A review of NDT/structural health monitoring techniques for hot gas components in gas turbines. *Sensors*. 2019;19(711):1–37. <https://doi.org/10.3390/s19030711>.
15. Park M, Hwang Y-h, Choi Y-s, Kim T-g. Analysis of a J69-T-25 engine turbine blade fracture. *Eng Fail Anal*. 2002;9:593–601. [https://doi.org/10.1016/S1350-6307\(02\)00003-1](https://doi.org/10.1016/S1350-6307(02)00003-1).
16. Mevissen F, Meo M. Ultrasonically stimulated thermography for crack detection of turbine blades. *Infrared Phys Technol*. 2022;122:104061. <https://doi.org/10.1016/j.infrared.2022.104061>.
17. Kukla D, Kopec M, Sitek R, Olejnik A, Kachel S, Kiskowskiak Ł. A novel method for high temperature fatigue testing of nickel superalloy turbine blades with additional NDT diagnostics. *Materials*. 2021;14:1392. <https://doi.org/10.3390/ma14061392>.
18. Tamarin Y. Protective coatings for turbine blades. Materials Park: ASM International; 2002. Ohio, USA
19. Dutta RS, Arya A, Yusufali C, Vishwanadh B, Tewari R, Dey GK. Formation of aluminides on Ni-based superalloy 690 substrate, their characterization and first-principle Ni(111)/NiAl(110) interface simulations. *Surf Coat Technol*. 2013;235:741–7. <https://doi.org/10.1016/j.surfcoat.2013.08.061>.
20. Zhang J, Liu W-d, Gong X-n, Yang Z-q, Zhou H-f, Xu Z-b, Zhang W-l. Probing the failure mechanisms and microstructure evolution of a high-pressure turbine blade coated with AlSiY. *Eng Fail Anal*. 2021;125:105436. <https://doi.org/10.1016/j.engfailanal.2021.105436>.
21. Dutta RS, Singh K, Vishwanadh B, Dey GK. Aluminide formation on Alloy 800 by plasma spraying and heat treatment. *Mater Manuf Process*. 2017;32(16):1845–50. <https://doi.org/10.1080/10426914.2017.1317794>.
22. Naraparaju R, Schulz U, Mechnich P, Döbber P, Seidel F. Degradation study of 7 wt.% yttria stabilised zirconia (7YSZ) thermal barrier coatings on aero-engine combustion chamber parts due to infiltration by different CaO–MgO–Al₂O₃–SiO₂ variants. *Surf Coat Technol*. 2013;235:741–7. <https://doi.org/10.1016/j.surfcoat.2013.08.061>.
23. Tacikowski M, Sitek R, Sikorski K, Wierzchoń T. Structure of Al–Ni intermetallic composite layers produced on the Inconel 600 by the glow discharge enhanced-PACVD method. *Intermetallics*. 2009;17(12):1098–104. <https://doi.org/10.1016/j.intermet.2009.06.010>.
24. Liu S-H, Trelles JP, Murphy AB, He W-T, Shi J, Li S, Li C-J, Li C-X, Guo H-B. Low-pressure plasma-induced physical vapor deposition of advanced thermal barrier coatings: microstructures, modelling and mechanisms. *Mater Today Phys*. 2021;21:100481. <https://doi.org/10.1016/j.mtphys.2021.100481>.
25. Kampe SL, Koss DA. The effect of stress state on the hydrogen embrittlement of Nickel. *Acta Metall*. 1999;34:895–900. [https://doi.org/10.1016/0001-6160\(86\)90231-2](https://doi.org/10.1016/0001-6160(86)90231-2).
26. Baskes MI, Vitek V. Trapping of hydrogen and helium at grain boundaries in nickel: an atomistic study. *Metall Mater Trans A*. 1985;16:1625–31. <https://doi.org/10.1007/BF02663018>.
27. Szczotok A, Kościelniak B. Characterization of IN 713C superalloy microstructure after high temperature creep test by LM, SEM and STEM. *Mater Eng*. 2016;2(210):50–58. <https://doi.org/10.15199/28.2016.2.1>.
28. Pierson HO. Handbook of chemical vapor deposition (CVD) principles, technology, and applications. 1999, William Andrew Pub., LLC Norwich, New York, U.S.A.
29. Yavorska M, Sieniawski J, Zielińska M. Functional properties of aluminide layer deposited on Inconel 713 LC Ni-based superalloy in the CVD process. *Arch Metall Mater*. 2011;56(1):187–92. <https://doi.org/10.2478/v10172-011-0022-z>.
30. Zhang G, Wang X, Xiong Y, Shi Y, Song J, Luo D. Mechanism for adsorption, dissociation and diffusion of hydrogen in hydrogen permeation barrier of α -Al₂O₃: a density functional theory study. *Int J Hydrog Energy*. 2013;38(2):1157–65. <https://doi.org/10.1016/j.ijhydene.2012.10.108>.
31. Yamabe J, Matsuoka S, Murakami Y. Surface coating with a high resistance to hydrogen entry under high-pressure hydrogen-gas environment. *Int J Hydrog Energy*. 2013;38(24):10141–54. <https://doi.org/10.1016/j.ijhydene.2013.05.152>.
32. Lu X, Ma Y, Wang D. On the hydrogen embrittlement behaviour of nickel-based alloys: Alloys 718 and 725. *Mater Sci Eng A*. 2020;792:139785. <https://doi.org/10.1016/j.msea.2020.139785>.
33. Kurniawan R, Park GC, Park KM, Zhen Yu, Kwak YI, Kim MC, Lee JM, Ko TJ, Park C-S. Machinability of modified Inconel 713C using a WC TiAlN-coated tool. *J Manuf Process*. 2020;57:409–30. <https://doi.org/10.1016/j.jmapro.2020.06.032>.
34. Orazem ME, Tribollet B. Electrochemical impedance spectroscopy. Hoboken: Wiley; 2008.
35. Kresse ZG, Furthmüller J. Efficiency of ab-initio total energy calculations for metals and semiconductors using a plane-wave basis set. *Comput Mater Sci*. 1996;6:15–50.
36. Kresse G, Furthmüller J. Efficient iterative schemes for ab initio total-energy calculations using a plane-wave basis set. *Phys Rev B*. 1996;54:11169.
37. Monkhorst HJ, Pack JD. Special points for Brillouin-zone integrations. *Phys Rev B*. 1976;13:5188.

38. Tuli V, Claisse A, Messina L, Burr PA. Solubility and vacancy-mediated interdiffusion in the Zr–Nb–Cr system. *J Nucl Mater.* 2021;548:152867. <https://doi.org/10.1016/J.JNUCMAT.2021.152867>.
39. Wldom B. Some topics in the theory of fluids. *J Chem Phys.* 1963;39:2808–12. <https://doi.org/10.1063/1.1734110>.
40. Voigt WA. Critical study of the elastic properties and stability of Heusler compounds: phase change and tetragonal X2YZ compounds. *Lehrbuch de Kristallphysik.* Leipzig: Terubner; 1928.
41. Reuss A. Berechnung der Fließgrenze von Mischkristallen auf Grund der Plastizitätsbedingung für Einkristalle. *ZAMM J Appl Math Mech.* 1929. <https://doi.org/10.1002/zamm.19290090104>.
42. Hill R. The elastic behaviour of a crystalline aggregate. *Proc Phys Soc A.* 1952;65:349–54.
43. Pugh SF. XCII. Relations between the elastic moduli and the plastic properties of polycrystalline pure metals. *Philos Mag.* 1954;7(45):823–43. <https://doi.org/10.1080/14786440808520496>.
44. Góral M, Pytel M, Filip R, Nowotnik A. The microstructure of hafnium modified aluminide coatings deposited by CVD method. *Mater Sci Forum.* 2015;844:172–6. <https://doi.org/10.4028/www.scientific.net/MSF.844.172>.
45. Zagórska M, Sitek R, Kamiński J, Matysiak H, Kurzydłowski KJ. Microstructure and corrosion resistance of Hf-modified NiAl layer on nickel superalloy Ni–Cr–Co–Mo–2Ti–1.5Al. *Mechanik.* 2015;2:307–15.
46. Tian WH, Han CS, Nemoto M. Precipitation of α -Cr in B2-ordered NiAl. *Intermetallics.* 1999;7:59–67.
47. Hinnemann B, Carter EA. Adsorption of Al, O, Hf, Y, Pt, and S atoms on α -Al₂O₃(0001). *J Phys Chem C.* 2007;111(19):7105–26. <https://doi.org/10.1021/jp068869c>.
48. Pan Z, Luo H, Zhao Q, Cheng H, Li X. Effect of Hf addition on microstructural evolution and corrosion behavior of nickel-based alloys in hydrochloric acid. *Corros Sci.* 2023;224:111507. <https://doi.org/10.1016/j.corsci.2023.111507>.
49. Maurya AK, Pandey SM, Chhibber R, et al. Structure–property relationships and corrosion behavior of laser-welded X-70/UNS S32750 dissimilar joint. *Arch Civ Mech Eng.* 2023;23:81. <https://doi.org/10.1007/s43452-023-00627-5>.
50. Maurya AK, Bhattacharyya A, Chhibber R, Pandey C. Structural integrity and corrosion behavior assessment of the dissimilar gas tungsten arc welded joint of sDSS 2507/IN625 superalloy. *Mater Chem Phys.* 2024;318:129322. <https://doi.org/10.1016/j.matchemphys.2024.129322>.
51. Jiang C. Site preference of transition-metal elements in B2 NiAl: a comprehensive study. *Acta Mater.* 2007;55(2007):4799–806. <https://doi.org/10.1016/J.ACTAMAT.2007.04.049>.
52. Eriş R, Akdeniz MV, Mekhrabov AO. The site preferences of transition elements and their synergistic effects on the bonding strengthening and structural stability of γ' -Ni₃Al precipitates in Ni-based superalloys: a first-principles investigation. *Metall Mater Trans A.* 2021;52:2298–313. <https://doi.org/10.1007/S11661-021-06222-8>.
53. Wang J, Shang S-L, Wang Y, Mei Z-G, Liang. Y-F, Du Y, Liu Z-K. First-principles calculations of binary Al compounds: enthalpies of formation and elastic properties. *Calphad.* 2011;35:562–73.
54. Sot R, Kurzydłowski KJ. Ab initio calculations of elastic properties of Ni₃Al and TiAl under pressure. *Mater Sci-Pol.* 2005;23(3):587–90.
55. Iotova D, Kioussis N, Lim SP. Electronic structure and elastic properties of the Ni₃X (X = Mn, Al, Ga, Si, Ge) intermetallics. *Phys Rev B Condens Matter.* 1996;54:14413–22. <https://doi.org/10.1103/PHYSREVB.54.14413>.
56. Boucetta S, Chihi T, Ghebouli B, Fatmi M. First-principles study of the elastic and mechanical properties of Ni₃Al under high pressure. *Mater Sci-Pol.* 2010;28(28):347–55.
57. Kim DE, Shang SL, Liu ZK. Effects of alloying elements on elastic properties of Ni₃Al by first-principles calculations. *Intermetallics.* 2010;18:1163–71. <https://doi.org/10.1016/j.intermet.2010.02.024>.

Publisher's Note Springer Nature remains neutral with regard to jurisdictional claims in published maps and institutional affiliations.

Authors and Affiliations

R. Sitek¹  · J. Kamiński¹ · A. Wadowski^{1,2} · M. Kopec³ · B. Adamczyk-Cieślak¹ · P. Bazarnik¹ · M. Drajewicz⁴ · W. J. Nowak⁴ · J. S. Wróbel¹

✉ R. Sitek
ryszard.sitek@pw.edu.p

¹ Faculty of Materials Science and Engineering, Warsaw University of Technology, Wołoska 141 Str., 02-507 Warsaw, Poland

² NOMATEN Centre of Excellence, National Center for Nuclear Research, Swierk, Otwock, Poland

³ Institute of Fundamental Technological Research, Polish Academy of Sciences, Pawińskiego 5B, 02-106 Warsaw, Poland

⁴ Department of Materials Science, Faculty of Mechanical Engineering and Aeronautics, Rzeszow University of Technology, al. Powstańców Warszawy 12, 35-959 Rzeszow, Poland